Journal of Alloys and Compounds 1010 (2025) 177081

Contents lists available at ScienceDirect

Journal of Alloys and Compounds

journal homepage: www.elsevier.com/locate/jalcom

Unveiling the magnetic structure of $BaFeO_{3-y}$: Shedding light on the elusive magnetic behavior

D. Gutiérrez-Martín [a], M. Hernando [a], M. Parras [a], A. Torres-Pardo [a], M.T. Fernández-Díaz [b,*], S. Savvin [b,c], J.M. González-Calbet [a], J.E. Rodrigues [d], R.S. Silva Jr [e], J.L. Martínez [e], A. Varela [a,*]

[a] Departamento de Química Inorgánica, Facultad de Ciencias Químicas, Universidad Complutense, Madrid 28040, Spain
[b] Institut Laue-Langevin, Grenoble 38042, France
[c] Instituto de Nanociencia y Materiales de Aragón, CSIC – Universidad de Zaragoza, Facultad de Ciencias C/ Pedro Cerbuna 12, Zaragoza, Spain
[d] CELLS-ALBA Synchrotron Light Source, Cerdanyola del Vallès, Barcelona 08290, Spain
[e] Instituto de Ciencia de Materiales de Madrid (ICMM), CSIC, Sor Juana Inés de la Cruz, 3. Cantoblanco, Madrid 28049, Spain

ARTICLE INFO

Keywords:
Structural study at low temperature
6H-$BaFeO_{2.96}$
Local oxidation state of iron
Magnetic properties
Magnetic structure

ABSTRACT

This work provides a comprehensive examination of the structural and magnetic properties of 6H-$BaFeO_{2.96}$ over a wide temperature range (10 K < T < 300 K) using neutron and synchrotron X-ray diffraction. Additionally, the local oxidation state of iron is examined using electron energy loss spectroscopy. No structural changes that could indicate a charge-order transition are observed in spite of a reported possible charge disproportionation of Fe^{4+} into $Fe^{(4+\delta)+}$ and $Fe^{(4-\delta)+}$ phenomenon at low temperature. According to the magnetic characterization, $BaFeO_{2.96}$ orders antiferromagnetically at T_N=156 K. The application of external magnetic fields strongly influences the magnetic behavior; the transition temperature shifts to lower values with the applied magnetic field and the long-range magnetic order melts with an applied field of 14 T. The magnetocaloric effect clearly shows at T_N a change from negative to positive magnetic entropy. The Rietveld refinement of the neutron powder diffraction data collected at 10 K, gives a magnetic ordering with propagation vector [0, 0, ½] and three magnetically distinct sites for the Fe atoms. This magnetic structure consists of ferromagnetic Fe-sheets perpendicular to the c-axis with the magnetic moments along the [110] direction coupled both ferromagnetic and antiferromagnetically along the c-axis. The magnetic moment values of the three Fe ions are very different evidencing a delicate equilibrium of competing magnetic interactions.

1. Introduction

The electronic properties of compounds containing unusually high valence ions have attracted much attention. In particular, oxides containing iron with oxidation states higher than (III) have been extensively investigated because they often exhibit valence transitions related to a certain charge instability that can be accompanied by significant variations in their structural or physical properties.

Perovskite-related oxides $CaFeO_3$ and $SrFeO_3$, prepared under oxidizing conditions, contain Fe in the IV oxidation state. Both cubic-$SrFeO_3$ [1,2] and orthorhombic-$CaFeO_3$ [3] present a spiral spin antiferromagnetic structure at 134 K and 115 K, respectively. However, the electronic behavior of tetravalent iron in both oxides is different. In $SrFeO_3$ the four-oxidation state is maintained at all temperatures, but not in $CaFeO_3$ which shows a charge disproportionation of $2Fe^{4+} \rightarrow Fe^{3+} + Fe^{5+}$ when cooled below 290 K [4]. These valence changes and/or disproportionation states cause significant modifications in their crystallographic structural (and physical) properties from orthorhombic *Pbnm* $GdFeO_3$ structure type (charge-delocalized state) to monoclinic $P2_1/n$ charge-disproportionated state. This second (or higher order) transition gradually occurs through the disproportionation process to $Fe^{4+\delta}$ and $Fe^{4-\delta}$ states with δ increasing when temperature decreases.

In contrast to the corner-sharing structures of the above mentioned oxides, the larger size of Ba ions leads to the stabilization of hexagonal polytypes, where octahedra corners-sharing alternate with faces-sharing octahedra, in different ratios, along the c-axis. At ambient pressure and high temperature, the $(cch)_2$-6H $BaFeO_{3-y}$ (y>0) polytype is obtained. Its structure is formed by $[Fe_2O_9]$ face-sharing dimers linked by single corner-sharing $[FeO_6]$ octahedra along the c-axis. On the other hand, at high pressures, a $(cchh)_3$-12R polytype is stabilized. This structure is

* Corresponding authors.
E-mail addresses: ferndiaz@ill.fr (M.T. Fernández-Díaz), aurea@ucm.es (A. Varela).

https://doi.org/10.1016/j.jallcom.2024.177081
Received 18 July 2024; Received in revised form 14 October 2024; Accepted 15 October 2024
Available online 16 October 2024

built up by trimers of face-sharing octahedra alternating, along the c-axis, with one corner sharing [FeO_6] unit. Besides, a fully oxidized cubic 3C-$BaFeO_3$ was obtained from the topotactic oxidation of cubic $BaFeO_{2.5}$ at low temperature.

Cubic 3C-$BaFeO_3$ presents a magnetic transition at 111 K from paramagnetic to A-type spin spiral order with a propagation vector along [100]. No charge disproportionation of the Fe^{4+} is reported [5].

On the contrary, fully oxidized hexagonal 12R-$BaFeO_3$, Fe^{4+} shows successive site-selective charge transition under cooling from 500 K to 4 K. At 500 K, two over three Fe^{4+} disproportionate ($2Fe^{4+} \rightarrow Fe^{3+} + Fe^{5+}$) giving rise to a structural change from rhombohedral (*R*-3*m*) to monoclinic (*C*2/*m*) symmetry. In a second transition, at 280 K, charge disproportionation of the remaining Fe^{4+} takes place, leading to a magnetic order of all iron spin. Finally, a charge interchange between Fe^{3+} and Fe^{5+} occurs at 50 K, which results in changes in the spin state and orientation [6].

Concerning the (*hcc*)-6H system, fully stoichiometric 6H-$BaFeO_3$ has been recently prepared by treating a $BaFeO_{3-y}$ phase under high-pressure and high-temperature conditions [7]. In air atmosphere, the stoichiometric phase is never attained and oxygen-deficient $BaFeO_{3-y}$, containing both Fe^{4+} and Fe^{3+}, is always obtained (y value strongly depends on the synthetic procedure). Regarding this point, previous works on the electronic and magnetic properties of this phase show discrepancies that can be ascribed to the oxygen stoichiometry that greatly affects final properties. The literature reports the magnetic and Mössbauer study of different oxygen-containing 6H-$BaFeO_{3-y}$ phases (ranging from $y = 0.28$–0.1), rendering the results hardly comparable. In spite of this, several works are devoted to the structural and magnetic study of 6H-phases of anionic composition around $BaFeO_{2.90}$.

H. Kobayashi et al [8]. measured the ^{57}Fe Mössbauer spectra for 6H-$BaFeO_{2.88}$ arguing that a magnetic order occurs at 130 K. Furthermore, they found that the Fe^{4+} concentration depends on the temperature decreasing from 170 K down to 4.2 K. Later, K. Mori et al [9] studied the structural changes in the composition 6H-$BaFeO_{2.91}$ over a wide temperature interval using neutron diffraction. At around 180 K, a weak distortion of the face-sharing octahedra is detected that could result from a partial disproportionation of Fe^{4+} in $Fe^{4+\delta}$ and $Fe^{4-\delta}$; however, no charge-ordering transition is reported, in contrast to the observation in $CaFeO_3$ or 12R-$BaFeO_3$.

On the other hand, the magnetic properties of this system have been extensively studied, but again with a clear dispersion and control on the oxygen content. S. Mori [10] first reports that the magnetic behavior of 6H-$BaFeO_{3-y}$ ($y < 0.1$) phases, which evidenced an AF-FM transition at 160 K. Later studies [11,12] have demonstrated that the magnetic state is paramagnetic in the range 160–220 K. Below 160 K, different interpretations of the magnetic state are reported. In the latest work [13], 6H-$BaFeO_{2.91}$ was studied using Time of Flight Small Angle Neutron Scattering (TOF-SANS). The results point out the existence of several magnetic states, a long-range antiferromagnetic ordering (below 130 K) coexisting with magnetic domains (short-range magnetic ordering) formed below 170 K. However, despite the large number of works related to the magnetic behavior of the 6H-phase, its magnetic structure is still unsolved.

In this work, we performed a comprehensive study of the magnetic and structural behavior of 6H-$BaFeO_{2.96}$, over a wide temperature range, by neutron and synchrotron X-ray diffraction. We also present the results of the magnetic susceptibility, heat specific, resistivity and magnetocaloric effect. Furthermore, we have prepared two different phases with lower oxygen content and higher Fe^{3+} content, $BaFeO_{2.90}$ and $BaFeO_{2.82}$, to establish the influence of the oxygen content, on magnetic, and thermal properties. A comparison of the magnetic behavior of these three 6 H phases is discussed.

2. Experimental section

2.1. Synthesis procedure

$BaFeO_{3-y}$ oxides were prepared by sol gel method as described in a previous work [14]. $Ba(NO_3)_2$ (5.23 g, Merck >99 %, CAS: 10022–31–8) and $Fe(NO_3)_2{\cdot}9\ H_2O$ (8.07 g, Merck ≥99.95 %, CAS: 7782–61–8)) were dissolved in 200 mL of deionized water. Citric acid monohydrate (8.40 g, Merck >99 %, CAS: 05949–29–1) and ethylene glycol (45 mL, Merck, CAS: 00107–21–1) were added to the solution under stirring and heating at (393 K). Then, the solution was further heated until complete evaporation and a dark brown solid was obtained. This precursor was manually ground and calcined at (623 K) overnight to remove organic residues. The obtained solid is treated at (1020 K) for 24 h to obtain the lowest oxygen content phase $BaFeO_{2.82}$. $BaFeO_{2.90}$ is obtained by oxidation of the previous sample at (473 K) under an ozone/oxygen flow (ca. 5 % O_3) for 4 h. Ozone was generated in situ by a Pacific Ozone L24 Ozone Generator. $BaFeO_{2.96}$ is obtained from $BaFeO_{2.82}$ at (1073 K) under an oxygen flow overnight. La_2LiFeO_6 was prepared by a previously described high-pressure method using a 20 % $LiNO_3$ excess [15].

The average cationic composition was determined using energy dispersive X-ray spectroscopy (EDS). The average oxidation state of iron was determined by a redox titration method from which the oxygen content is estimated. Samples were dissolved in HCl (6 N) with an excess of $Fe(NH_4)_2SO_4.6H_2O$ (Mohr salt). The Fe^{2+} ions react with the possible Fe^{4+} present in the sample, leading to Fe^{3+} ions. The amount of remaining Fe^{2+} ions was then determined by titration with a 0.1 N $K_2Cr_2O_7$ solution.

2.2. Neutron diffraction (ND)

The neutron diffraction data were collected on two diffractometers at the Institute Laue-Langevin [16]. The high-intensity diffractometer D20 a wavelength of $\lambda = 2.42$ Å was used to collect data between 7 and 146 K, to follow the evolution of the magnetic ordering. On this instrument, the evolution of the structure was also followed measuring between 50 and 300 K with a wavelength of $\lambda = 1.54$ Å. The final experiment was carried out on the high-intensity diffractometer XtremeD to obtain data of the low angle magnetic peaks by using a wavelength of $\lambda = 3.82$ Å. In the three experiments, approximately 2 g of polycrystalline sample powder was loaded into a 9-mm-diameter vanadium can placed in an orange cryostat. The data were analyzed with the Rietveld method[17] using the software package FullProf [18].

2.3. Synchrotron X-ray diffraction (SXRD)

High-resolution synchrotron X-ray diffraction patterns were acquired at the ESRF beamline ID22 (European Synchrotron Radiation Facility, Grenoble). The incident radiation employed a wavelength set to $\lambda = 0.42775$ Å. Low-temperature data collection in the range of 100–280 K utilized a LN_2-based cryostream. Powder samples were encapsulated and sealed in borosilicate capillaries with a diameter of 0.5 mm, and rotational motion was applied to enhance data statistics. Diffraction patterns were captured over the 2θ 1–40° range using a multi-analyzer stage consisting of 13 Si(111) crystals [19]. Rietveld refinements were carried out utilizing the FullProf program, employing a pseudo-Voigt function to describe the peak shape. The refinement encompassed the optimization of various parameters, including scale factors, zero-point error, background coefficients, asymmetry-correction factors, lattice parameters, atomic positions, occupancy factors, isotropic displacement parameters, and preferential orientation.

2.4. Electron energy loss spectroscopy (EELS)

Electron energy loss spectroscopy (EELS) experiments were acquired using a GIF-QuantumER with a collection semiangle of 18 mrad and a

convergence semiangle of 20.3 mrad. The Fe oxidation state was analyzed from the energy-loss near edge fine structure (ELNES) of Fe−$L_{2,3}$ signals. ELNES spectra were acquired over ~0.5 nm area with energy dispersion of 0.25 eV and 2.5 mm spectrometer aperture. The total acquisition time was optimized to prevent beam damage to the sample. The dual-EELS function of the GIF-QuantumER spectrometer, allowing the simultaneous acquisition of two different energy ranges, was used to record simultaneously zero-loss peak (0.0001 s exposition time, 10 frames) and Fe−$L_{2,3}$ core region to minimize the uncertainty on the energy shift of the Fe−$L_{2,3}$ edges. Low-temperature EELS was performed using a double tilt (±24°) liquid nitrogen-cooled specimen holder Gatan 636.

2.5. Specific heat and resistivity measurements

Specific heat measurements were conducted on a Physical Properties Measurement System (PPMS) from Quantum Design (San Diego, USA) by the heat pulse-relaxation method. The temperature range expands from 2 up to 360 K and the range of applied magnetic field is up to 9 T. The sample was attached to a specific sample holder made of sapphire, with Apiezon grease N. The sample holder plate is equipped with a calibrated heater and calibrated Cermox thermometers. After a heat pulse is applied to the system, the measurement of the temperature relaxation is converted into the heat capacity of the sample, after the subtraction of the heat capacity added by the addenda grease. The resistivity measurements were performed on the same PPMS system by the four contacts mode. The electrical contacts were directly attached to the sample pellet by means of a silver paste.

2.6. Magnetic characterization

The magnetic susceptibility and magnetization were measured with a MPMS-3S SQUID magnetometer from Quantum Design (San Diego, USA), in a temperature range from 1.8 up to 400 K and applied magnetic fields up to 7 T. An oven composed of a Al_2O_3 ceramic stick with a resistance and a thermocouple embedded in the ceramic is used for these measurements. Such a furnace is able to increase the temperature from 300 to 1000 K, inside the cryostat system of the magnetometer. The sample is placed in contact to the alumina ceramic surface and glued by a high temperature cement. Some complementary data at higher magnetic fields (up to 14 T) were measured in the Vibrating Sample Magnetometer (VSM) option for the PPMS from Quantum Design (San Diego, USA).

3. Results and discussion

3.1. Structural behavior

3.1.1. Neutron diffraction (ND) of 6H-$BaFeO_{2.96}$ under cooling

The starting point of this work was the refinement of the $(hcc)_2$-6H-$BaFeO_{3-y}$ structure by ND and SXRD at room temperature. ND refinement at room temperature [20] confirms the 6 H structure ($P6_3/mmc$ space group) and gives a slight deficiency on the O1 sites, resulting in $BaFeO_{2.96}$ net composition.

The 6H-$BaFeO_{2.96}$ structure is formed by face-sharing Fe2 octahedra dimers linked by an isolated Fe1 octahedron sharing vertices (Fig. 1). According to the different cation sizes of Fe^{III} (r=0.645 Å(HS)) and Fe^{IV} (r=0.585 Å) [21] the small fraction of Fe (III) should occupy the largest Fe1 site leading to the unit formula $Ba(Fe^{III}_{0.08}Fe^{IV}_{0.25})(Fe^{IV}_{0.66})O_{2.96}$. The neutron diffraction data at 300 K, unveils that Fe2 atoms shift away from the center of the octahedron towards the cubic Fe1-layer, with respect to the ideal 6H-polytype, reducing electrostatic repulsion between neighboring Fe^{IV} cations within adjacent face-sharing octahedra. This displacement leads to three longer Fe2-O1 distances (2.014(3) Å) and three shorter Fe2-O2 distances (1.862(5) Å) distorting the dimer octahedra. This is a common feature observed in other hexagonal polytypes with face and corner shared octahedra units.

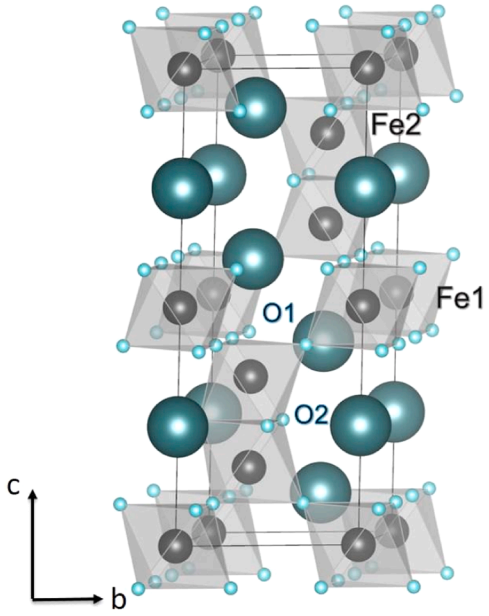

Fig. 1. Structure model of the $(hcc)_2$-6H-$BaFeO_{2.96}$ [20].

The possible structural and magnetic transitions below room temperature were investigated by neutron diffraction measurements. Data were collected over different temperature values between 50 and 300 K in a D20 diffractometer at λ=1.54 Å. In the temperature dependent ND patterns, from RT to 160 K, no significant structural changes were observed (Fig. 2a). Neither additional maxima appear, nor the width of certain reflections increases indicating that the hexagonal symmetry does not change. Below 150 K extra peaks appear in the ND patterns that cannot be accounted for by nuclear scattering and are attributed to magnetic Bragg scattering resulting from long-range magnetic order (Fig. 2b).

All diffraction data were successfully analyzed with the 6 H structure model obtained at 300 K. As expected, the unit-cell parameters over the 50–300 K temperature range, decrease with decreasing temperature according to the lattice thermal contraction effect as the temperature is reduced.

The structural parameters were carefully analyzed at each measured temperature. Fig. 3a, b and c depict the thermal dependence of the Fe-O distance values. No abrupt change at any temperature is found. They tend to decrease as the temperature decreases with minor fluctuations that are within the experimental error of the obtained values (±0.003). These results do not reproduce those of K. Mori [9] who observed a break in the variation of these distances at 170 K. These authors suggest that this weak octahedra distortion results from a charge disproportionation of Fe^{4+} into $Fe^{(4+\delta)+}$ and $Fe^{(4-\delta)+}$ phenomenon. However, atomic pair distribution function (PDF) data, determined by neutron scattering experiments [22], agree with our results since the PDF pattern remains unchanged at temperatures lower than 170 K, indicating that iron's local structure is not modified with decreasing temperature.

Several works have focused on the study by Mössbauer spectroscopy of the electronic state of Fe in the 6H-$BaFeO_{3-y}$ system since H. Kobayashi [8] reported that the Fe^{4+} concentration decreases with decreasing temperature in 6H-$BaFeO_{2.88}$. The origin of this feature seems to be in the Fe^{4+} disproportionation process that takes place gradually, starting from around 170 K and extending down to 4 K [9].

At 170 K, the extent of such disproportionation is small, and as a consequence not enough to induce observable changes in the structural parameters. Therefore, the Fe-O distances can be expected to remain constant, as observed in Fig. 3. Furthermore, based on the different sizes of the Fe^{III}, Fe^{IV} and Fe^{V}, a charge-redistributing process along

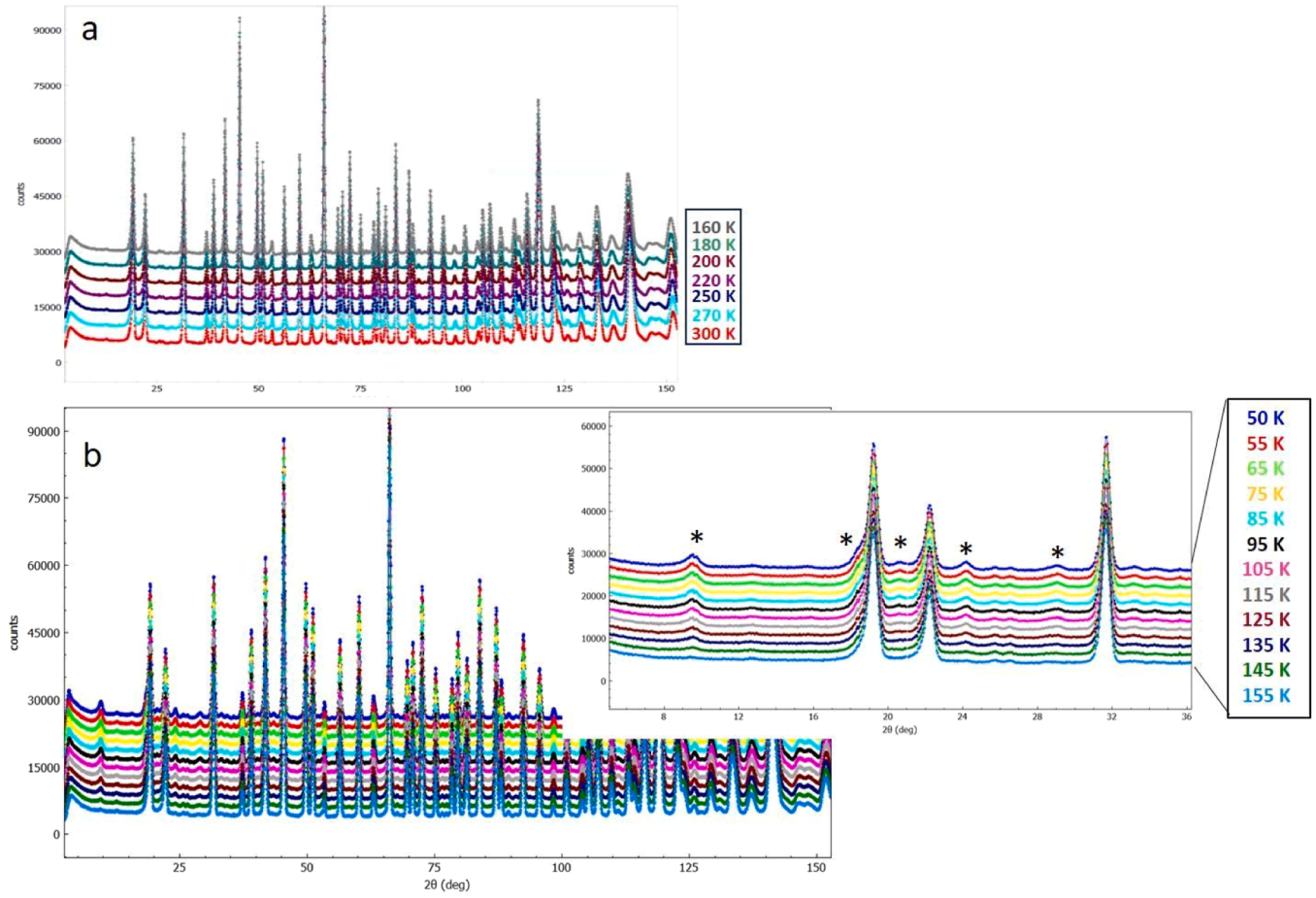

Fig. 2. Temperature-dependent neutron powder diffraction patterns for $BaFeO_{2.96}$. **(a)** From 300 K down to 160 K and **(b)** From 155 K down to 50 K. Selected region of the NDP (0 °<2θ<36 °) between 155 and 50 K is shown in the inset. Magnetic peaks are marked with asterisks.

disproportionation could occur, in such a way that $Fe^{(4+\delta)+}$ will likely occupy the smaller octahedral sites (face-sharing octahedra), while $Fe^{(4-\delta)+}$ and Fe^{4+} would coexist in the larger octahedra (corner-sharing dimers). However, it is noteworthy that the Fe-Fe distance within the dimer remains constant (2.77 Å) in the same temperature range [21]. This is an interesting point considering that an expansion of the Fe-Fe distance could be anticipated, as the amount of $Fe^{4+\delta}$ increases in an attempt to mitigate electrostatic repulsions. This result suggests that the structural framework of the hexagonal 6 H perovskite at room temperature exhibits remarkable stability, being able to accommodate $Fe^{4\pm\delta}$ cations of different sizes, without inducing abrupt structural changes.

Changes in the electronic states of transition metal oxides can lead to significant changes in their structural properties when a charge order is established. As mentioned above, this is the case for $CaFeO_3$ or 12R-$BaFeO_3$ which undergo symmetry change from orthorhombic to monoclinic in the former, and from hexagonal to monoclinic symmetry in the latter. In both cases, this structural change is caused by the $2Fe^{4+}\rightarrow Fe^{3+} + Fe^{5+}$ charge disproportion and ordering in different crystallographic sites of the structure. In our experimental data of the 6H-$BaFeO_{2.96}$ phase, no structural change is detected by ND. In this regard, it should be noticed that a similar partial charge disproportionation of Ni^{3+} into $Ni^{(3+\delta)+}$ and $Ni^{(3-\delta)+}$ has been found in orthorhombic $RENiO_3$ perovskites (RE: Y, Pr-Lu). This process is accompanied by a structural change from orthorhombic to monoclinic symmetry that is not always easily detectable.

3.1.2. Synchrotron X-ray diffraction (SXRD)

In view of this, we have used SXRD to further analyze the temperature evolution of the 6H-structure in $BaFeO_{2.96}$. The results of SXRD pattern refinements obtained in the temperature range 90–280 K are shown in Figs. S1 a and b in SI while structural parameters and interatomic distances are gathered in Tables S1 and S2, respectively. All the temperature-dependent diffraction data have been refined with the 6 H structure type ($P6_3/mmc$ space group), without observing any extra maxima or/and reflection splitting, which could suggest a structural transition at temperatures below 170 K. Moreover, as depicted in Fig. S2, the refinement results do not show sudden discontinuities in the lattice parameters with temperature. Therefore, we can conclude that the partial Fe^{4+} charge disproportionation in 6H-$BaFeO_{2.96}$ does not involve a charge-ordered structural change.

In Fig. 4a, the thermal evolution of the unit-cell volume for 6H-$BaFeO_{2.96}$ is presented from SXRD data. It is clear that the volume behaves in accordance with expectations from a Debye's solid description. The thermal expansion of the unit-cell volume was characterized using the Grüneisen model for the zero-pressure equation of state, with its first-order expansion, as described elsewhere[23,24]. The model is expressed as follows:

$$V_{cell}(T) = V_0 + \frac{9\gamma N k_B T}{B_0}\left(\frac{T}{\theta_D}\right)^3 \int_0^{\frac{\theta_D}{T}} \frac{x^3 dx}{e^x - 1} \quad (1)$$

where, V_0 signifies the unit-cell volume at 0 K, θ_D represents the Debye temperature, N denotes the number of atoms in the unit cell (= 30), B_0 stands for the isothermal bulk modulus, and γ is the Grüneisen parameter.

We compare the experimental volume expansion with the best fitted curve using Eq. (1). The fitting results in $V_0 = 384.23$ Å^3, $\theta_D \sim 506$ K, and $\gamma/B_0 = 1.22\times10^{-11}$ Pa^{-1}. In fact, the obtained Debye temperature is

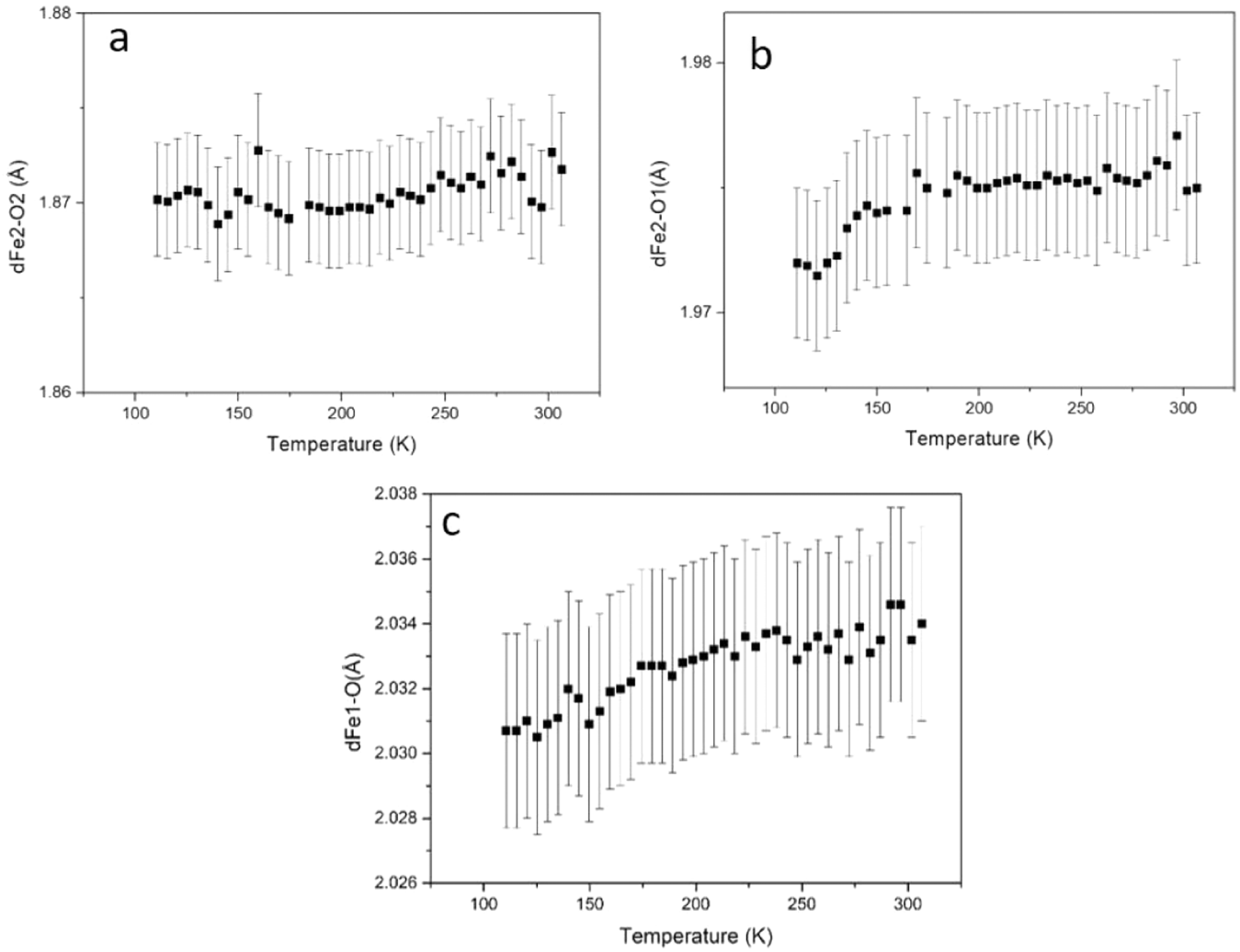

Fig. 3. Temperature dependence of Fe-O distance values (Å): **(a)** Fe2-O2, **(b)** Fe2-O1 and **(c)** Fe1-O2.

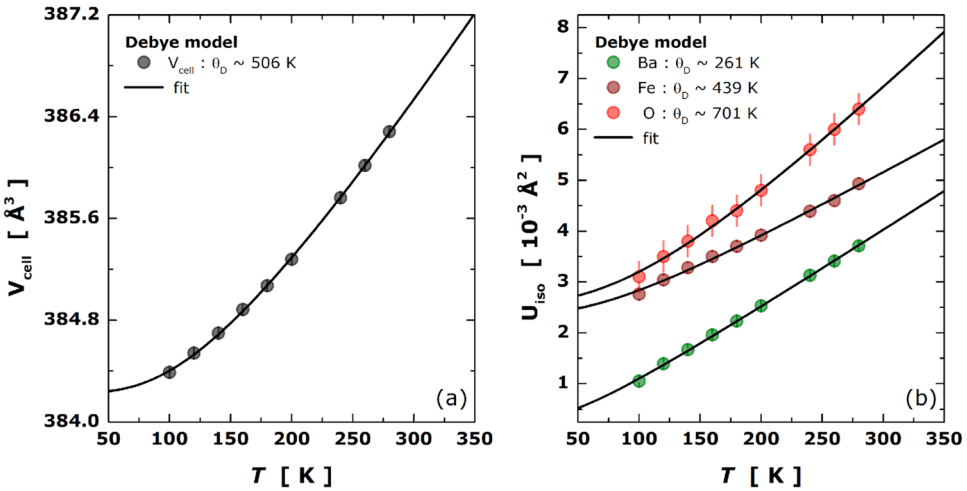

Fig. 4. Temperature variation of the: **(a)** unit-cell volume (V_{cell}) and **(b)** the experimental U_{iso} values extracted from the Rietveld refinement of the SXRD data.

in good agreement with the values obtained for other perovskite-based systems, such as $SrTiO_3$[25], $BaZrO_3$[26], and $CaGeO_3$[27].

The lack of any discernible anomaly in the volume around the magnetic transition at ~170 K may suggest that, if a magnetoelastic coupling occurs, it should appear at a local level. The analysis of individual atomic oscillations can be conducted by determining the mean square displacements (U_{iso}), using the next equation [27]:

$$U_{iso}(T) = d_0^2 + \frac{3\hbar^2 T}{m k_B \theta_D^2}\left[\frac{\theta_D}{4T} + \frac{T}{\theta_D}\int_0^{\theta_D/T}\frac{x}{e^x - 1}dx\right] \quad (2)$$

such that, d_0^2 signifies the intrinsic disorder and m represents the atomic mass.

In Fig. 4b, the experimental U_{iso} values, extracted from the Rietveld refinement for Ba, Fe, and O atoms, are shown together with respective fitting derived from Eq. (2). One may notice the good agreement and the absence of any anomaly around the magnetic transition temperature in 6H-$BaFeO_{2.96}$. The best fitting of the experimental U_{iso} to the Debye model in Eq. (2) provides θ_D values of 261, 439, and 701 K for Ba, Fe, and O, respectively. These Debye values can be used for estimating the bonding stiffness through the harmonic one-particle potential (OPP) [28]: $K = \frac{mk_B^2\theta_D^2}{3\hbar^2}$. Here, K stands for the force constant (in units of eV/Å^2), yielding values of 5.5, 6.4, and 4.6 eV/Å^2 for the Ba, Fe, and O, respectively. These values exhibit an increasing order as follows $K_O < K_{Ba} < K_{Fe}$, meaning that has Fe-O pairs has a more covalent nature than the Ba-O bonds.

3.1.3. *Electron energy-loss near edge spectroscopy (ELNES)*

As mentioned above, the hyperfine parameters measured by Mössbauer spectroscopy change with temperature suggesting that Fe^{4+}, $Fe^{(4+\delta)+}$ and $Fe^{(4-\delta)+}$ coexist below 170 K[8]. In an attempt to analyze these electronic changes, at a local level, we have performed a study by EELS.

Fe-$L_{2,3}$ EELS data have been extensively discussed in the literature from iron-based compounds with Fe(II), Fe(III), and Fe(IV) oxidation states [13,24]. Although the detection of Fe(V) has been reported by XANES, no experimental data from Fe(V) $L_{2,3}$ edge has been reported, as far as we know, by electron energy-loss near edge spectroscopy (ELNES). We report here for the first time EELS Fe $L_{2,3}$ spectra of iron with oxidation state (V). The ELNES Fe $L_{2,3}$ signals of inorganic solids with Fe (V) complement the previously reported Fe $L_{2,3}$ ELNES collection for Fe (II), Fe(III), and Fe(IV) [20,29]. These data provide valuable information for the elucidation of Fe oxidation states in inorganic solids.

ELNES spectra at Fe $L_{2,3}$ edge for iron oxides with different oxidation states are plotted in Fig. 5. The absolute energy of each Fe $L_{2,3}$ edge was precisely calibrated with the zero-loss signal simultaneously acquired (further described in the experimental methods section), while the conditions were optimized to avoid beam damage. A clear variation in the shape and the energy position is observed as a function of the Fe oxidation state.

We have used Fe_2O_3, Ba_2FeO_4, and La_2LiFeO_6 compounds as references, containing Fe (III), Fe (IV), and Fe (V), respectively, with octahedral [FeO_6] units like those observed in the present $BaFeO_{2.96}$ sample. The synthetic procedure of the La_2LiFeO_6 phase is detailed in SI. The Fe $L_{2,3}$ edge corresponding to the La_2LiFeO_6 material is visibly shifted to higher energy loss values and reveals different shapes for the Fe (III) and Fe (IV) signals (see Table S3 in SI). Fe(V) oxidation state for La_2LiFeO_6 has been determined by Mössbauer spectroscopy [30] thus the EELS Fe-$L_{2,3}$ signal acquired from La_2LiFeO_6 can be associated to iron with Fe(V) oxidation state.

At room temperature, the EELS Fe $L_{2,3}$ edges of Ba_2FeO_4 and $BaFeO_{2.96}$ sample (depicted with a blue line in Fig. 5a) are very similar, with very close $I(L_3)/I(L_2)$ ratios, as well as energy loss positions of the L_3 and L_2 lines (see Table S3 in SI). Therefore, we confirm that the majority of the iron of $BaFeO_{2.96}$ presents IV oxidation state at room temperature.

To gain direct insight to a possible variation of the Fe oxidation state for the $BaFeO_{2.96}$ material below 170 K, we resort to EELS studies employing an *in-situ* cooling sample holder. The Fe-$L_{2,3}$ edge spectra of $BaFeO_{2.96}$ acquired 105 K (red line) together with the Fe-$L_{2,3}$ edges acquired from the reference materials described above are represented in Fig. 5b. No major changes are observed between the signals of $BaFeO_{2.96}$ acquired at 105 K and 293 K, except from the clear improvement of the signal-to-noise ratio as the temperature decreases (see Fig. S3 in SI) and, consequently, a sharping of the low-temperature Fe-$L_{2,3}$ edge would be expected for the data recorded at 105 K. Notice that the difference between the energy values of Fe(III)-L_2 and Fe(V)-L_2 signals is limited to 2.5 eV. Despite the narrow energy window, a subtle broadening is noticeable in the Fe-L_2 signal acquired at 105 K for the $BaFeO_3$ sample, when compared to the signal obtained at room temperature (see Fig. S4 in SI). This phenomenon can be ascribed to the presence of two shoulders (highlighted with a star in Fig. 5(b)), flanking the central peak at 711.7 eV assigned to the Fe(IV) signal. The observed broadening may be compatible with a certain degree of disproportionation of Fe (IV) consistent with Mössbauer results [8].

3.2. *Thermal, magnetic and transport characterization*

The specific heat data for $BaFeO_{2.96}$ is presented in Fig. 6 in a temperature range from 5 to 180 K. The experimental data at 0 T clearly shows a broad peak around 156 K, that can be associated with a phase transition.

In the temperature range from 50 K to 300 K, the specific heat is mostly affected by two components: the phonons (crystal lattice) and the

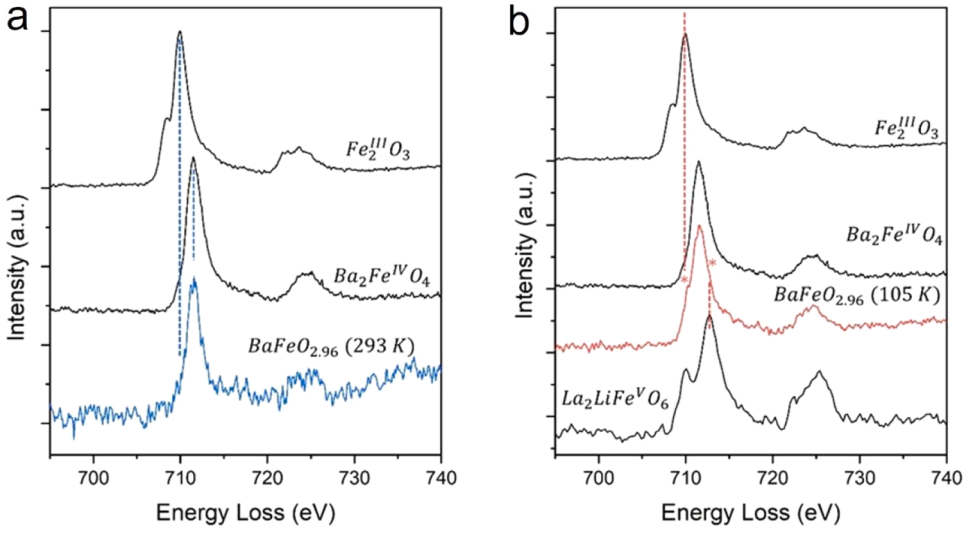

Fig. 5. (a) ELNES Fe-$L_{2,3}$ edges form references with Fe^{III} (Fe_2O_3) and Fe^{IV} (Ba_2FeO_4) oxidation states (black lines) and $BaFeO_{2.96}$ sample acquired at 293 K (blue line). **(b)** ELNES Fe-$L_{2,3}$ edge of reference La_2LiFeO_6 with Fe^{V} oxidation state completes the ELNES Fe-$L_{2,3}$ edges of references with Fe^{III} and Fe^{IV} (black lines). ELNES Fe-$L_{2,3}$ edge from $BaFeO_{2.96}$ acquired at 105 K (red line) shows two shoulders (marked with stars) causing the broadening of the Fe-$L_{2,3}$ edge.

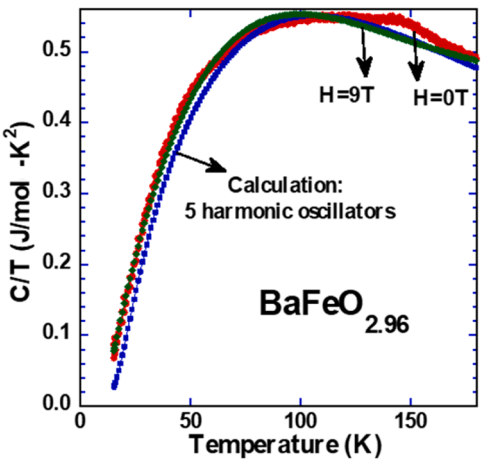

Fig. 6. Temperature dependence of $BaFeO_{2.96}$ specific heat for an external magnetic field of $H = 0$ T (red) and $H = 9$ T (green). The calculation of the specific heat with a model of five harmonic oscillators is included (blue).

magnetic contribution (long-range magnetic structure), which need to be separated in order to extract the pure magnetic contribution. In a first approximation, we could simulate the phonon contribution by pure harmonic oscillators, centered at different frequencies (temperatures). The simulation of C/T produced by 5 harmonic oscillators centered at frequencies equivalents to 90, 190, 320, 550, and 910 K is presented in Fig. 6 and perfectly matches the experimental C/T values at 90 and 180 K. A second alternative, is to apply a strong external magnetic field to saturate the magnetic moments from well above the ordering temperature. This strong magnetic field will make the entropy associated with the magnetic phase transition to be spread out over a wide temperature range.

This effect is observed in the experimental data of C/T with $\mu_0 H = 9$ T and presented also in Fig. 6. Both approaches (harmonic oscillators and external magnetic field) coincide and a direct subtraction of either one, from the experimental C/T data at $\mu_0 H = 0$ T, produces the magnetic component of the specific heat $(\Delta C/T)_{Mag}$ for $BaFeO_{2.96}$. The data of the magnetic component of the specific heat after the subtraction of the $(C/T)_{9\,T}$ is presented in Fig. S5. The temperature dependence of the $(\Delta C/T)_{Mag}$ shows a clear peak at T_N=156 K, probably associated with a magnetic phase transition. This phase transition is displaced to lower temperatures, when an external magnetic field is applied and almost disappears for $\mu_0 H$ above 7 T.

The integration of the magnetic component of the specific heat is related to the magnetic entropy associated with the phase transition, following:

$$S_M(T) = \int_0^T \left(\frac{\Delta C}{T}\right)_{Mag} dT \qquad (3)$$

The value obtained is only around 0.7 J/mol K, which is much smaller than theoretically expected (2R ln $(2S+1)$ = 26.7 J/mol K), but much closer to the relative magnetic entropy obtained by the magnetocaloric effect (~1.2 J/mol K) explored later on the manuscript (see below). This discrepancy between the calculated magnetic entropy and the experimental one could be indicative of severe magnetic frustration in this compound [31].

Finally, the temperature dependence of the resistivity was measured in a pellet of $BaFeO_{2.96}$, as presented in Fig. S6. The sample presents a semiconductor behavior from low temperature to 400 K. The semiconductor behavior of the electrical conductivity is well described by an activation energy of 1.2 eV, as presented in Fig. S6. The electrical behavior is coherent with the one observed by Gil de Muro *et al,* [32] although a metallic behavior was expected from the temperature dependence from their ESR data. No anomalies in the resistivity of the sample were observed at temperatures close to T_N. In principle, the explanation for this lack of anomalies in the resistivity seems to be related to the process of producing a pellet, from the powder sample, the different densities (as a consequence of the grain boundaries and connectivity) and the high sensitivity of the magnetic and transport properties on the slight changes of the oxygen stoichiometry in this compound.

The magnetic susceptibility data as a function of temperature is presented in Fig. 7. The measurements were performed in two steps, the first from 2 to 310 K in the normal cryostat sample holder and the second from 310 up to 500 K in the specific sample holder to be inserted in the oven of the magnetometer. The two sets of data perfectly match despite the difference in the sample holders and the corresponding background signals.

The analysis of the paramagnetic (PM) region (300–500 K) is rather linear and could fit to a Curie-Weiss behavior ($\chi^{-1} = \frac{T-\Theta}{C}$). The extracted PM moment ($\mu \approx \sqrt{8C}$) in this wider temperature range is 2.9 μ_B/Fe atom. Also, the Curie-Weiss temperature (Θ) obtained from this linear behavior is $\Theta = +135$ K, indicating mostly FM-like short-range magnetic interactions between the Fe ions in this PM regime.

These values are rather parcel, since the expected (calculated) PM effective moment for Fe^{4+} is around 4.9 μ_B/Fe atom in the high spin state (4 unpaired electrons) or 3.0 μ_B/Fe atom in the low spin state, with only 2 unpaired electrons. From that data we could argue that the Fe^{4+} is in the low spin state with only 2 unpaired electrons. Moreover, the magnetic susceptibility, shown in Fig. 7, with a clear sharp peak around 156 K and almost no difference in the process of zero field cooling/field cooling (not shown in this figure) seems to indicate an antiferromagnetic (AFM) phase transition. The field dependence of the magnetization in $BaFeO_{2.96}$ (Fig. 8) also adds some information. The low temperature (2 K) field-dependent magnetization, with saturation up to 14 T (not shown in this figure), indicates a double hysteresis loop-like behavior, with a saturation magnetization around 0.6 μ_B/Fe atom and linear behavior of the magnetization around $\mu_0 H = 0$ T. This behavior is consistent with an AFM ordering at low temperature.

We have also measured the magnetic susceptibility under the same conditions (heating after the same process of field cooling), but with different applied magnetic fields. The results are presented in Fig. 9, where the temperature dependence of the magnetic susceptibility is presented in a wide range of applied magnetic fields from 0.01 up to 14 T.

The peak related to the long-range AFM order ($T_N = 156$ K) strongly depends on the applied magnetic field, with a strong decrease in the

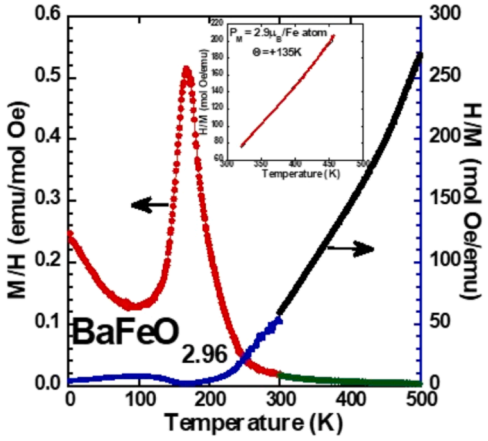

Fig. 7. Temperature dependence of the magnetic susceptibility and the inverse susceptibility for $BaFeO_{2.96}$ measured with an applied magnetic field of 0.01 T. The inset shows the linear fitting of the inverse magnetic susceptibility in the range 320–465 K, with the corresponding values of the paramagnetic moment and Curie-Weiss temperature.

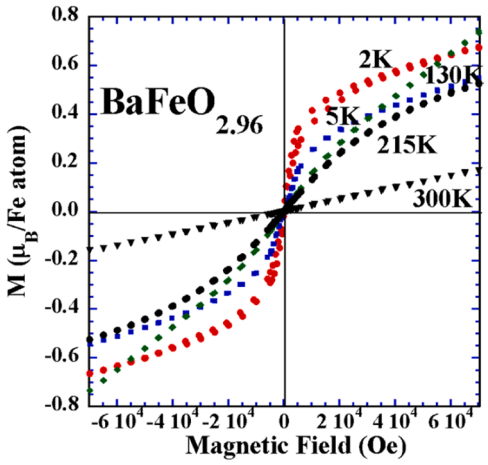

Fig. 8. Isothermals of the magnetic field dependence of the magnetization for $BaFeO_{2.96}$ at different temperatures between 2 and 300 K.

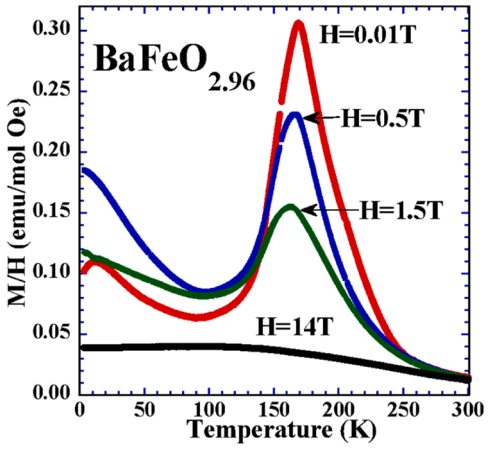

Fig. 9. Temperature dependence of the magnetic susceptibility of $BaFeO_{2.96}$ for different applied magnetic fields of 0.01, 0.5, 1.5 and 14 T. The data at 14 T was measured in a VSM magnetometer and the data at 1.5 T was measured after in a Zero Field Cool.

peak height of the magnetic susceptibility, and a shift to lower temperatures even for relatively weak fields (0.5 and 1.5 T). This behavior completely coincides with the observed dependence of the peak in the specific heat under the application of external magnetic fields (see above). When higher magnetic fields are applied (14 T), the peak in the magnetic susceptibility disappears and the long-range ordering seems to be suppressed down to the lowest measured temperature. This melting of the long-range magnetic ordering by an external magnetic field, in a compound showing a honeycomb network of Fe ions with competing magnetic interactions, is a particularly interesting phenomenon deserving a deeper study out of the scope of this work.

We believe that the apparent inconsistency in the published results on this compound is due to the great influence of oxygen vacancies. To corroborate this, we prepared $BaFeO_{3-y}$ samples with different oxygen content (y) and consequently, different amounts of vacancies. The magnetic susceptibility and the magnetic field dependence of the magnetization for $y = 0.10$ ($BaFeO_{2.90}$) and for $y = 0.18$ ($BaFeO_{2.82}$) are presented in Figs. S7a and b. The obtained results are discussed in SI. This study points out again that the introduction of vacancies in the structure of $BaFeO_3$ produces strong perturbations in the exchange magnetic interaction and as a consequence the magnetic ordering is significantly affected.

To complement the study of the $BaFeO_{2.96}$ sample, we performed a magnetocaloric effect (MCE) analysis by the magnetic entropy change (ΔS_M) as a function of temperature. Several isotherms $M(H)$ curves on the 2–260 K (with $\Delta T = 3$ K steps) temperature range were collected in applied magnetic fields up to 7 T, as presented in Fig. 10a.

The curve (in Fig. 10a) exhibits a convex and elongated type shape up to the saturation tendency below T_N, and a PM behavior above T_N. Noticeably, a crossover temperature-dependent behavior could be observed which is well consistent with a step-like metamagnetic transition from AFM to FM-like state, not observed in previous studies[33]. To visualize clearly this feature, the isotherm $M(H)$ has been transformed into Arrott plot (H/M vs M^2) [34] as displayed in Fig. 10b. According to M. Mizumaki et al. [35], a typical positive slope corresponding to a second-order magnetic transition is expected for $BaFeO_{2.96}$. We observe clear evidence of first-order magnetic transition (negative slope of some curves) occurrence, as highlighted in the inset of Fig. 10b. Interestingly, the reduced $BaFeO_{2.82}$ sample (see Fig. S8a-d in SI), reveals a second-order magnetic transition related to a superparamagnetic state or FM-like ordering.

From the $M(H)$ isotherms, temperature-dependent ΔS_M was calculated using the approximated following relation:

$$\Delta S_M(T, H_0) = \sum_i \frac{M_{i+1} - M_i}{T_{i+1} - T_i} \Delta H_i, \tag{4}$$

where, M_i and M_{i+1} are the experimental data obtained at T_i and T_{i+1} under a magnetic field H_i, respectively [34]. Fig. 10c shows the $\Delta S_M(T)$ curves for $BaFeO_{2.96}$ sample under selected magnetic fields up to $\Delta H =$ 0–7 T. As expected, the magnitude of $\Delta S_M(T)$ increases continuously with ΔH increasing. In agreement with Arrott plot analysis, a crossover in ΔS_M as temperature increases is observed, i.e., from inverse MCE (negative $-\Delta S_M$ value between ~70–160 K) to conventional MCE (positive $-\Delta S_M$ value) behavior. As a result, the negative peak value of $-\Delta S_M$ ($-\Delta S_M^{max}$ at 0–7 T) for related to inverse MCE, is obtained to be −2.1 J/kg K, whereas the positive peak around T_N, related to conventional MCE, is obtained to be 0.9 J/kg K. The same features are observed for $y = 0.1$ ($BaFeO_{2.90}$) sample (see Fig. S9a). On the contrary, in the most reduced $BaFeO_{2.82}$ sample (Fig. S9b), the inverse MCE is suppressed and only a positive $-\Delta S_M^{max}$ value, related to conventional MCE, is found. These results are shown (Figs. S9 a-d) and discussed in SI.

3.3. Magnetic structure from neutron diffraction

Neutron diffraction patterns recorded below 160 K contain scattering contributions to the Bragg peaks that could be of magnetic origin, as previously discussed. At this point, it is noticeable that despite the relatively large amount of works referring to the magnetic structure feature of 6H-$BaFeO_{3-y}$ phase over more than twenty years, this structure has remained unsolved until now. In this work, a plausible magnetic structure is proposed for the first time.

We have attempted to refine the data obtained on the D20 diffractometer ($\lambda = 2.42$ Å) assuming an incommensurate magnetic structure along the c-axis with [0,0,0.45] propagation vector suggested by Mori et al [9]. From this, a complex spiral magnetic structure emerges like that reported by $CaFeO_3$ [4]. However, the low-temperature magnetic data cannot be fitted satisfactorily with such model. In our low-temperature data, we could observe the occurrence of a strong magnetic signal at low Q, but the lowest accessible angle on D20 instrument did not permit us to determine the position and the intensity of this peak accurately. To obtain well-defined magnetic peaks we recorded neutron diffraction data on XtremeD diffractometer (ILL, Grenoble) using λ=3.8 Å at 10 K. The positions of the measured magnetic peaks allowed us to define a propagation vector [0,0, ½] for this commensurate magnetic structure (see Fig. S10 in SI).

The magnetic symmetry analysis was performed using the suite of programs on Magnetic Symmetry and Applications of the Bilbao Crystallographic server [36]. Running k-SUBGROUPSMAG we can obtain the

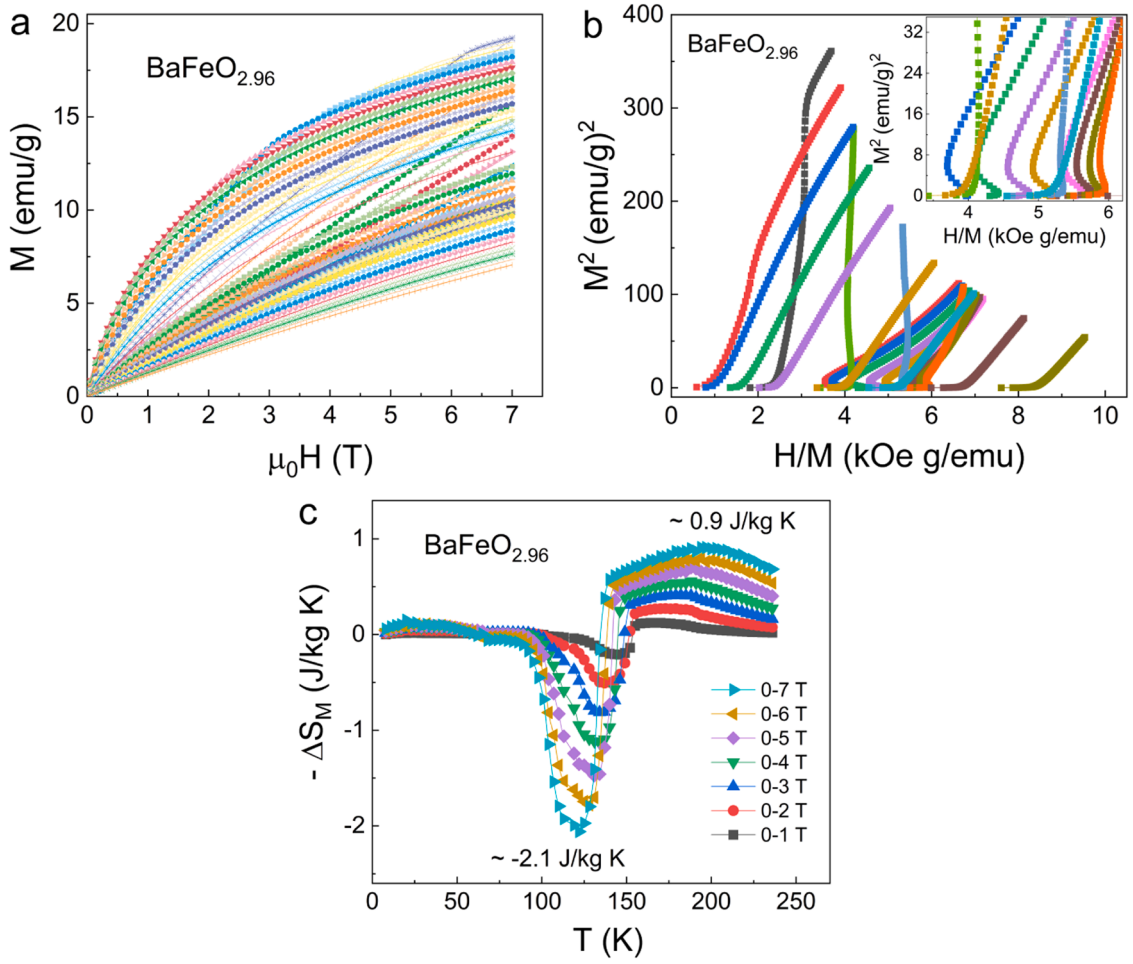

Fig. 10. **(a)** Isotherm $M(H)$ curve on the 2–260 K temperature range in the applied magnetic fields up to 7 T for $BaFeO_{2.96}$ sample **(b)** Arrott plot (H/M vs M^2) constructed from $M(H)$ curve for the same sample. Inset shows a highlight of this behavior. **(c)** $\Delta S_M(T)$ curve for the $BaFeO_{2.96}$ sample under selected magnetic fields up to 0–7 T.

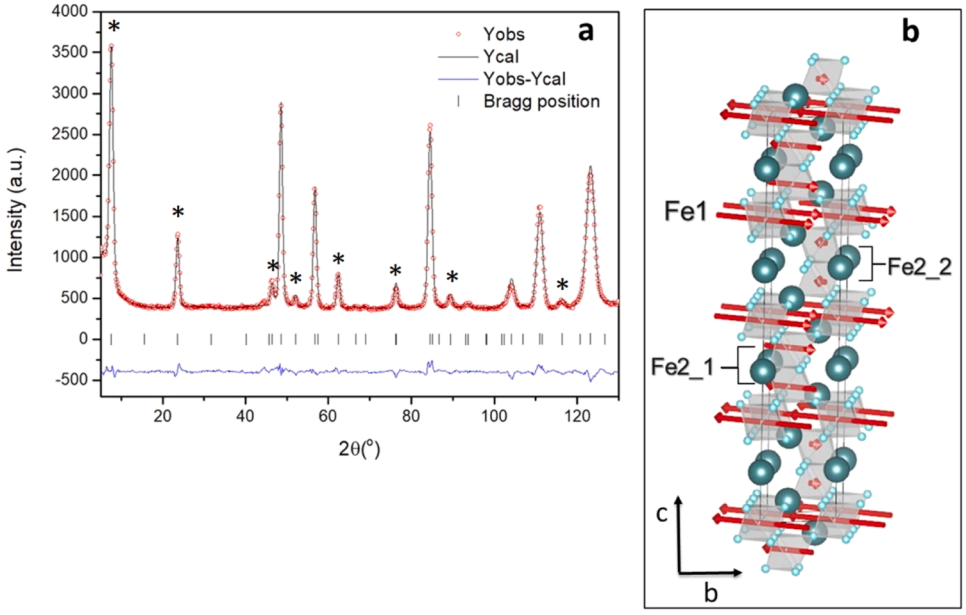

Fig. 11. **(a)** Neutron diffraction data with Rietveld refinement on $BaFeO_{2.96}$ at 10 K. The red dots represent observed data (Io) and the black line represents the Rietveld fit to the data (IC). The green tics are the allowed nuclear and magnetic reflections (marked with asterisks), (Bragg R-factor: 4.30). **(b)** Magnetic structure of $BaFeO_{2.96}$ at 10 K.

possible subgroups for the parent space group $P6_3/mmc$ (No. 194) and the propagation vector k = [0, 0, ½] and their hierarchical graph is shown in Fig. S11 in the supporting information.

Even if one should start by exploring the groups with the highest symmetry, when considering the Wyckoff positions occupied by the Fe magnetic atoms, the high-symmetry 2*a* (0,0,0) for Fe1 and the special position 4*f* (1/3,2/3,z) for Fe2, it becomes rapidly clear that the symmetry has to be decreased to explain the experimental data. Out of four maximal magnetic space groups, two impose all the Fe atoms to have zero magnetic moment, and the other two only allow magnetic moments along the z direction. Those cannot explain the observed magnetic ordering, as the first and strongest magnetic peak at 7.9 degrees (Fig. 11a) corresponds to the (001) reflection, which cannot be justified by a model without spin components contained within the (001) plane, i.e. perpendicular to the scattering vector. This is also the case for some of the second level groups in the group-subgroup hierarchy depicted in Fig. S10, where Fe atoms either bear no magnetic moment at all or have it aligned exclusively along the z direction.

The systematic test of the possible orderings allowing components of the magnetic moments perpendicular to the z direction, gives satisfactory refinements of neutron data only for two magnetic space group, i.e. A_amm2 (#38.192) and the A_ama2 (#40.208), both of them being polar groups. For these groups, following the procedure implemented in MAXMAGN, using the Belov-Neronova-Smirnova (BNS) notation [37], the paramagnetic basis (a,b,2c; 0,0,0) has been transformed to the standard BNS cell using the transformation (−c,a+b,a-b; 0,0,7/8). The lowered symmetry of the two space groups results in the splitting of the Fe2 atoms into two sites: Fe2_1 and Fe2_2, while Fe1 does not undergo any splitting. The main difference between both magnetic models is that for the first, A_amm2 (#38.192) the possible components of the magnetic moments for the three Fe atoms take the form (m_x, m_x, 0), while for the second, A_amm2 (#40.208) they are of the form (m_x, -m_x, m_z). The neutron diffraction data collected at 10 K were refined by considering simultaneously the nuclear and magnetic phases and the magnetic moments at the three Fe sites were refined independently for both of the above magnetic models. The refinement in the A_amm2 (#38.192) group results in a plausible magnetic model. The same refinement with the space group A_ama2 (#40.208) does not give an improved solution as the variation of the m_z component is very small and unstable and when fixed to zero, the resulting model is the same as the one with A_amm2 (#38.192) group within a shift in z direction.

Fig. 11a presents the final Rietveld refinement against the neutron data collected at 10 K and the corresponding magnetic structure is given in Fig.11b. The Table S4 in SI summarizes the components of the magnetic moments.

The ordered moment of Fe1 at 10 K is 3.97(5) μ_B, bigger than those for Fe2 atoms which are 2.08(5) μ_B for Fe2_1 and 0.50(2) μ_B for Fe2_2. These values are all smaller than the free ion values corresponding to Fe^{IV} (4.89 μ_B), Fe^{III} (5.91 μ_B), and Fe^{V} (3.87 μ_B) although they are comparable to the reported in the literature for samples with Fe in such oxidation state[4,38]. The ordered magnetic moment of Fe2_2 is close to zero indicating a strong frustration resulting from the competing interactions. These results are consistent with the fact that the environments around Fe1 and Fe2 are markedly different. Fe1 atoms are at the center of undistorted corner-sharing octahedra with equal Fe-O distances of 2.023(1) Å, while the face-sharing octahedral surrounding Fe2 atoms present three shorter distances of 1.877(1) Å and three longer of 1.957 Å.

The resulting magnetic structure presents some interesting features. It consists of ferromagnetic sheets perpendicular to the c-axis with the magnetic moments along the [110] direction. However, different types of coupling, i.e. ferro or antiferromagnetic, can be found between the Fe layers along the c-axis. A ferromagnetic coupling exists between Fe1 and Fe2_1, whereas an antiferromagnetic one is present between Fe1 and Fe2_2. In addition, an AF coupling between the Fe2_1 and a ferromagnetic coupling between the Fe2_2 is observed within the dimers. According to the Kanamori-Goodenough [39] rules only an AF coupling between Fe is expected in 6H-$BaFe^{III-IV}O_{3-x}$ due to ~180° and ~90° Fe-O-Fe superexchange interactions. The diverse nature of the magnetic interactions found in this magnetic structure denotes the existence of charge fluctuations and a possible segmented bond network created by the oxygen vacancies. The reduced value of the magnetic moment and the semiconducting character of our sample indicate a significant degree of covalence between the Fe and O atoms. As a result, a delicate equilibrium between double-exchange ferromagnetic interactions competing with a frustrated network of different superexchange interactions takes place. Moreover, due to this intricate competition of interactions, we cannot rule out the possibility of some more complicated magnetic structure that could be revealed by single crystal measurements.

4. Conclusions

We have performed a study of the structural and magnetic transitions of the 6H-$BaFeO_{2.96}$ sample over a wide temperature range (10–300 K) using powder-diffraction (neutron/ synchrotron) and spectroscopy techniques (EELS). No significant structural changes were found either by ND nor by high resolution SXRD. All the temperature-dependent diffraction patterns have been refined with the 6 H structure type ($P6_3/mmc$ space group). No extra maxima or/and reflection splitting, which could suggest a structural transition at temperatures below 170 K are observed.

The Fe electronic changes, at a local level, have been analyzed by *in situ* EELS between 300 and 105 K. No major changes are observed between the signals of $BaFeO_{2.96}$ acquired at 105 K and 293 K. As references, besides the Fe(III)-$L_{2,3}$ and Fe(IV)-$L_{2,3}$ spectra, EELS Fe(V)-$L_{2,3}$ is presented for the first time. When the sample is cooled to 105 K, a slight broadening of the Fe-L_2 signal, compared to that taken at room temperature, is observed despite the small energy difference between the Fe (III)-L_2 and Fe(V)-L_2 values. This broadening points out to that a partial disproportionation process of Fe^{4+} into $Fe^{(4+\delta)+}$ and $Fe^{(4-\delta)+}$. At 105 K the extent of such disproportionation should be small, and therefore, not enough to induce observable changes in the structural parameters of the 6H-phase. Through the disproportionation process, $Fe^{(4-\delta)+}$ likely occupies the corner-sharing octahedra while $Fe^{(4+\delta)+}$ and Fe^{4+} would coexist in the face-sharing dimers without inducing abrupt structural changes in the structural framework of the hexagonal 6 H perovskite.

From the bulk transport, thermal and magnetic measurement we conclude that $BaFeO_{2.96}$ orders antiferromagnetically at T_N=156 K. The introduction of oxygen vacancies in the 6H-structure induces a clear frustration in the magnetic interactions, with the corresponding influence in the magnetic susceptibility and magnetization. The entropy associated with this magnetic transition from the specific heat and magnetocaloric effect is lower than expected probably related to the complex magnetic structure, where different Fe sites are associated with very different magnetic moments. The magnetocaloric effect revealed a transition of inverse to conventional magnetic entropy change -ΔS_M near T_N as temperature increases.

From neutron diffraction data at 10 K, a plausible magnetic structure has been proposed for 6H-$BaFeO_{2.96}$. The magnetic structure is commensurate with a propagation vector [0,0,1/2] and three magnetically different Fe sites (Fe1, Fe2_1 and Fe2_2). This model consists of ferromagnetic Fe-sheets perpendicular to the c-axis with the magnetic moments along the [110] direction coupled both ferromagnetic and antiferromagnetically along the c-axis. The values of the ordered magnetic moment in the three Fe sites are very different; 3.97(5) μ_B for Fe1 atoms, 2.08(5) μ_B for Fe2_1 and 0.50(2) μ_B for Fe2_2. The covalence between the Fe and O atoms can give rise to a complicated competition of ferro and antiferromagnetic interactions, resulting in a high degree of frustration in the magnetic structure of this compound.

Funding Sources

We acknowledge the support from the "(MAD2D-CM)-UCM" project funded by Comunidad de Madrid, by the Recovery, Transformation and Resilience Plan, and by Next Generation EU from the European Union and from the Ministerio de Ciencia, Innovación y Universidades through Research Projects PID2020–113753RB-I00 and TED2021–129254B-C22. DGM acknowledges financial support from CT63/19-CT64/19 Complutense fellowship and A.T.P. acknowledges the Comunidad de Madrid for the PR65/19–22438 Research Project.

CRediT authorship contribution statement

A. Varela:Writing – review & editing, Writing – original draft, Visualization, Supervision, Methodology, Conceptualization. **D. Gutiérrez-Martín**:Writing – review & editing, Writing – original draft, Visualization, Methodology, Investigation. **R. S. Silva Jr.**:Writing – original draft, Investigation, Formal analysis. J. L. Martínez:Writing – review & editing, Writing – original draft, Investigation, Formal analysis. **J. M. González-Calbet**:Writing – original draft, Resources, Funding acquisition. **J. E. Figueiredo Soares**:Writing – original draft, Investigation, Formal analysis. **M.T. Fernández-Díaz**:Writing – review & editing, Writing – original draft, Investigation, Formal analysis. **S. Savvin**:Writing – review & editing, Investigation. **Marina Parras**: Writing – review & editing, Writing – original draft, Visualization, Supervision, Methodology, Conceptualization. **A. Torres-Pardo**:Writing – review & editing, Writing – original draft, Investigation, Formal analysis. **María Hernando**:Writing – original draft, Investigation, Formal analysis

Declaration of Competing Interest

The authors declare that they have no known competing financial interests or personal relationships that could have appeared to influence the work reported in this paper.

Acknowledgment

We thank J.A. Alonso for useful discussions of the SXRD results. J.E. F.S.R. thanks the ESRF scientific and technical staff for the synchrotron X-ray diffraction measurements at ID22-ESRF (proposal: MA-5678). We thank the National Facility ELECMI ICTS and CAI for XRD (UCM) for the facilities. We acknowledge the ILL and the Spanish CRG XtremeD for the allocation of neutron beam time. D.G.M. acknowledges ELECMI (proposal ELC178–2023) for the allocation of aberration corrected microscope time.

Appendix A. Supporting information

Supplementary data associated with this article can be found in the online version at doi:10.1016/j.jallcom.2024.177081.

Data Availability

Data will be made available on request.

References

[1] Y. Takeda, M. Shimada, F. Kanamaru, M. Koizumi, N. Yamamoto, Magnetic properties and mossbauer effect IN 12-layer hexagonal BaFeO 3, Mat. Res. Bull. 9 (1974) 537–544.
[2] T. Takeda, R. Kanno, Y. Kawamoto, M. Takano, S. Kawasaki, T. Kamiyama, F. Izumi, Metal-semiconductor transition, charge disproportionation, and low-temperature structure of Ca 1-x Sr x FeO 3 synthesized under high-oxygen pressure, 2000. www.elsevier.com/locate/ssscie.
[3] F. Kanamaru, H. Miyamoto, Y. Mimura, M. Koizumi, Synthesis of a new perovskite CafeO3, Mat. Res. Bull. 5 (1970) 257–262, https://doi.org/10.1016/0025-5408(70)90121-2.
[4] P.M. Woodward, D.E. Cox, E. Moshopoulou, A.W. Sleight, S. Morimoto, Structural studies of charge disproportionation and magnetic order in CaFeO 3, Phys. Rev. B 62 (2000) 844–855.
[5] N. Hayashi, T. Yamamoto, H. Kageyama, M. Nishi, Y. Watanabe, T. Kawakami, Y. Matsushita, A. Fujimori, M. Takano, BaFeO3: a ferromagnetic iron oxide, Angew. Chem. Int. Ed. 50 (2011) 12547–12550, https://doi.org/10.1002/anie.201105276.
[6] Z. Tan, F. Denis Romero, T. Saito, M. Goto, M. Amano Patino, A. Koedtruad, Y. Kosugi, W.T. Chen, Y.C. Chuang, H.S. Sheu, J.P. Attfield, Y. Shimakawa, Charge disproportionation and interchange transitions in twelve-layer BaFe O3, Phys. Rev. B 102 (2020), https://doi.org/10.1103/PhysRevB.102.054404.
[7] R. Watanabe, M. Goto, Y. Kosugi, D. Kan, Y. Shimakawa, Oxygen release and incorporation behaviors in $BaFeO_3$ polymorphs with unusually high-valence Fe^{4+}, Chem. Mater. (2024) https://doi.org/10.1021/acs.chemmater.3c03236.
[8] H. Kobayashi, Y. Nishihara, Study on the hexagonal BaFeO3-y system by the Mössbauer effect, Nucl. Instrum. Methods Phys. Res. 76 (1993) 258–259.
[9] K. Mori, T. Kamiyama, H. Kobayashi, K. Oikawa, T. Otomo, S. Ikeda, Structural evidence for the charge disproportionation of Fe4+ in BaFeO3-δ, J. Phys. Soc. Jpn. 72 (2003) 2024–2028, https://doi.org/10.1143/JPSJ.72.2024.
[10] S. Mori, Magnetic Properties of several phases of Barium orthoferrate BaFeOx, J. Phys. Soc. Jpn. 28 (1970) 44–50.
[11] F. Iga, Y. Nishihara, T. Katayama, K. Murata, Y. Takeda, Magnetic and transport properties of BaFeO3-y, J. Magn. Magn. Mater. 104–107 (1992) 1973–1975, https://doi.org/10.1016/0304-8853(92)91628-7.
[12] F. Iga, Y. Nishihara, G. Kido, Y. Takeda, Mössbauer effect and high-field magnetization of BaFeO3-y, J. Magn. Magn. Mater. 104–107 (1992) 1969–1972.
[13] K. Mori, T. Kamiyama, H. Kobayashi, T. Otomo, K. Nishiyama, M. Sugiyama, K. Itoh, T. Fukunaga, S. Ikeda, Mixed magnetic phase in 6H-type BaFeO3-δ, J. Appl. Crystallogr 40 (2007) 501–505, https://doi.org/10.1107/S0021889807001653.
[14] A. el Hadri, I. Gómez-Recio, E. del Río, J.C. Hernández-Garrido, R. Cortés-Gil, M. Hernando, Á. Varela, Á. Gutiérrez-Alonso, M. Parras, J.J. Delgado, J.A. Pérez-Omil, G. Blanco, J.J. Calvino, J.M. González-Calbet, Critical influence of redox pretreatments on the CO oxidation activity of $BaFeO_{3-\delta}$ perovskites: an in-depth atomic-scale analysis by aberration-corrected and in situ diffraction techniques, ACS Catal. 7 (2017) 8653–8663, https://doi.org/10.1021/acscatal.7b02595.
[15] G. Demazeau, B. Buffat, F. Mènil, L. Fournés, M. Pouchard, J.M. Dance, P. Fabritchnyi, P. Hagenmuller, Characterization of coordinated iron (V) in an oxide lattice, Mat. Res. Bull. 16 (1981) 1465–1472, https://doi.org/10.1016/0025-5408(81)90067-2.
[16] Hernando M., M.T. Fernández-Díaz, Influence of Redox Pre-Treatments on the CO Oxidation Activity of BaFeO3-d: Relationship between Catalytic Activity and Structural Features, Institute Laue-Langevin (ILL) (2016). https://doi.org/DOI: 10.5291/ILL-DATA.5-24-599.
[17] H.M. Rietveld, A profile refinement method for nuclear and magnetic structures, J. Appl. Crystallogr 2 (1969) 65–71, https://doi.org/10.1107/S0021889869006558.
[18] J. Rodríguez-Carvajal, Recent advances in magnetic structure determination by neutron powder diffraction, Phys. B Phys. Condens. Matter 192 (1993) 55–69, https://doi.org/10.1016/0921-4526(93)90108-I.
[19] A. Fitch, C. Dejoie, E. Covacci, G. Confalonieri, O. Grendal, L. Claustre, P. Guillou, J. Kieffer, W. De Nolf, S. Petitdemange, M. Ruat, Y. Watier, ID22 - the high-resolution powder-diffraction beamline at ESRF, J. Synchrotron Radiat. 30 (2023) 1003–1012, https://doi.org/10.1107/S1600577523004915.
[20] D. Gutiérrez-Martín, A. Varela, M. Hernando, A. Torres-Pardo, E. Matesanz, I. Gómez-Recio, J.M. González-Calbet, M.T. Fernández-Díaz, J.J. Calvino, M. A. Cauqui, M.P. Yeste, M. Parras, Exploring reversible redox behavior in the 6H-$BaFeO3-\delta$ ($0 < \delta < 0.4$) System: impact of Fe3+/Fe4+ ratio on CO oxidation, Inorg. Chem. 63 (2024) 8908–8918, https://doi.org/10.1021/acs.inorgchem.4c00917.
[21] R.D. Shannon, Revised effective ionic radii and systematic studies of interatomie distances in halides and chalcogenides, Acta Crystallogr. A 32 (1976) 751–767, https://doi.org/10.1107/S0567739476001551.
[22] K. Mori, T. Kamiyama, H. Kobayashi, K. Itoh, T. Otomo, S. Ikeda, Local structure of BaFeO3-δ studied by neutron scattering, Phys. B Condens Matter (2003) 807–808, https://doi.org/10.1016/S0921-4526(02)02571-1.
[23] J.E.F.S. Rodrigues, J. Gainza, F. Serrano-Sánchez, R.S. Silva, C. Dejoie, N. M. Nemes, O.J. Dura, J.L. Martínez, J.A. Alonso, Thermal expansion and rattling behavior of Gd-filled Co4Sb12 Skutterudite determined by high-resolution synchrotron X-ray diffraction, Materials 16 (2023), https://doi.org/10.3390/ma16010370.
[24] L. Vočadlo, K.S. Knight, G.D. Price, I.G. Wood, Thermal expansion and crystal structure of FeSi between 4 and 1173 K determined by time-of-flight neutron powder diffraction, Phys. Chem. Min. 29 (2002) 132–139, https://doi.org/10.1007/s002690100202.
[25] B. Luo, X. Wang, E. Tian, G. Li, L. Li, Electronic structure, optical and dielectric properties of BaTiO3/CaTiO3/SrTiO3 ferroelectric superlattices from first-principles calculations, J. Mater. Chem. C Mater. 3 (2015) 8625–8633, https://doi.org/10.1039/c5tc01622c.
[26] K.S. Knight, Low-temperature thermophysical and crystallographic properties of BaZrO3 perovskite, J. Mater. Sci. 55 (2020) 6417–6428, https://doi.org/10.1007/s10853-020-04453-5.
[27] A. Nakatsuka, A. Yoshiasa, K. Fujiwara, O. Ohtaka, Variable-temperature single-crystal X-ray diffraction study of SrGeO3 high-pressure perovskite phase, J. Mineral. Petrol. Sci. 113 (2018) 280–285, https://doi.org/10.2465/jmps.180605.

[28] J.E.F.S. Rodrigues, C.A. Escanhoela, B. Fragoso, G. Sombrio, M.M. Ferrer, C. Álvarez-Galván, M.T. Fernández-Díaz, J.A. Souza, F.F. Ferreira, C. Pecharromán, J.A. Alonso, Experimental and theoretical investigations on the structural, electronic, and vibrational properties of Cs2AgSbCl6 double perovskite, Ind. Eng. Chem. Res. 60 (2021) 18918–18928, https://doi.org/10.1021/acs.iecr.1c02188.
[29] H. Tan, J. Verbeeck, A. Abakumov, G. Van Tendeloo, Oxidation state and chemical shift investigation in transition metal oxides by EELS, Ultramicroscopy 116 (2012) 24–33, https://doi.org/10.1016/j.ultramic.2012.03.002.
[30] J.H. Choy, G. Demazeau, S.H. Byeon, Stabilization of Fe(V) as substituting element in the La2LiVO 6 perovskite, Solid State Commun. 77 (1991) 647–649.
[31] R.C. Sahoo, S. Das, T.K. Nath, Influence of magnetic frustration and structural disorder on magnetocaloric effect and magneto-transport properties in La1.5Ca0.5CoMnO6 double perovskite, J. Appl. Phys. 123 (2018), https://doi.org/10.1063/1.5004600.
[32] I.G. De Muro, M. Insausti, L. Lezama, T. Rojo, Effect of the synthesis conditions on the magnetic and electrical properties of the BaFeO3-x oxide: a metamagnetic behavior, J. Solid State Chem. 178 (2005) 1712–1719, https://doi.org/10.1016/j.jssc.2005.03.028.
[33] K. Yoshii, N. Hayashi, M. Mizumaki, M. Takano, Magnetocaloric effect of Sr-substituted BaFeO3 in the liquid nitrogen and natural gas temperature regions, AIP Adv. 7 (2017), https://doi.org/10.1063/1.4982244.
[34] R.S. Silva, J. Gainza, C. dos Santos, J.E.F.S. Rodrigues, C. Dejoie, Y. Huttel, N. Biskup, N.M. Nemes, J.L. Martínez, N.S. Ferreira, J.A. Alonso, Magnetoelastic coupling and cryogenic magnetocaloric effect in two-site disordered GdSrCoFeO6 double perovskite, Chem. Mater. 35 (2023) 2439–2455, https://doi.org/10.1021/acs.chemmater.2c03574.
[35] M. Mizumaki, K. Yoshii, N. Hayashi, T. Saito, Y. Shimakawa, M. Takano, Magnetocaloric effect of field-induced ferromagnet BaFeO3, J. Appl. Phys. 114 (2013), https://doi.org/10.1063/1.4818316.
[36] J.M. Perez-Mato, S.V. Gallego, E.S. Tasci, L. Elcoro, G. De La Flor, M.I. Aroyo, Symmetry-based computational tools for magnetic crystallography, Annu Rev. Mater. Res. 45 (2015) 217–248, https://doi.org/10.1146/annurev-matsci-070214-021008.
[37] N.V. Belov, N.N. Nerova, T.S. Smirnova, The 1651 Schubnikov grops, Sov. Phys. Crystallogr. 2 (1957) 311.
[38] Z. Tan, A. Koedtruad, M. Goto, M. Iihoshi, Y. Shimakawa, Layered hexagonal perovskite oxides 21R Ba7Fe5Ge2O20and 12H Ba6Fe3Ge3O17, Inorg. Chem. 60 (2021) 1257–1263, https://doi.org/10.1021/acs.inorgchem.0c03423.
[39] J.B. Goodenough, Magnetism and the Chemical Bond, New York, 1963.